Article

Cell Reports

Emergent Orientation Selectivity from Random Networks in Mouse Visual Cortex

Graphical Abstract

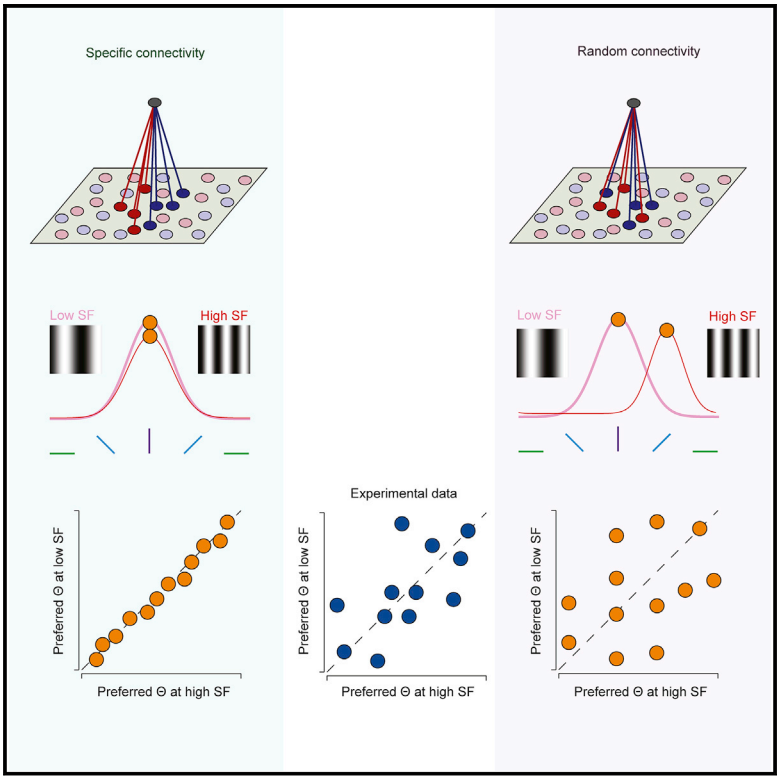

Authors

Jagruti J. Pattadkal, German Mato, Carl van Vreeswijk, Nicholas J. Priebe, David Hansel

Correspondence

david.hansel@parisdescartes.fr

In Brief

Pattadkal et al. show that orientation selectivity can emerge from random connectivity, and offer a distinct perspective for how computations occur in the neocortex. They propose that a random convergence of inputs can provide signals for orientation preference in contrast with the dominant model that requires a precise arrangement.

Highlights

- Random connectivity explains orientation selectivity in visual cortex
- Preferred orientation depends on spatial frequency

Pattadkal et al., 2018, Cell Reports *24*, 2042–2050
August 21, 2018
https://doi.org/10.1016/j.celrep.2018.07.054

CellPress

OPEN ACCESS
CellPress

Cell Reports
Article

Emergent Orientation Selectivity from Random Networks in Mouse Visual Cortex

Jagruti J. Pattadkal,[1] German Mato,[2] Carl van Vreeswijk,[3] Nicholas J. Priebe,[1,4] and David Hansel[3,4,5,*]
[1]Center for Perceptual Systems and Center for Learning and Memory, The University of Texas at Austin, 2415 Speedway, Austin, TX 78712, USA
[2]Centro Atomico Bariloche and Instituto Balseiro, CNEA and CONICET, 8400 Bariloche, Rio Negro, Argentina
[3]Center of Neurophysics, Physiology and Pathologies, CNRS-UMR8119, 45 Rue des Saints-Pères, 75270 Paris, France
[4]Senior author
[5]Lead Contact
*Correspondence: david.hansel@parisdescartes.fr
https://doi.org/10.1016/j.celrep.2018.07.054

SUMMARY

The connectivity principles underlying the emergence of orientation selectivity in primary visual cortex (V1) of mammals lacking an orientation map (such as rodents and lagomorphs) are poorly understood. We present a computational model in which random connectivity gives rise to orientation selectivity that matches experimental observations. The model predicts that mouse V1 neurons should exhibit intricate receptive fields in the two-dimensional frequency domain, causing a shift in orientation preferences with spatial frequency. We find evidence for these features in mouse V1 using calcium imaging and intracellular whole-cell recordings.

INTRODUCTION

Since its initial description by Hubel and Wiesel (1962), orientation selectivity has served as a platform for studying neocortical computations (Priebe and Ferster, 2012). V1 neurons in primates and carnivores are characterized not only by their preference for the orientation of bars or edges but also by the preference for a bar or edge of a specific orientation being invariant to the spatial structure of the object displayed. For example, a V1 neuron that responds best to a vertical orientation should maintain that orientation preference despite changes in the width or movement of a presented bar (De Valois et al., 1982; Jones et al., 1987; Webster and De Valois, 1985).

Orientation selectivity emerges in V1 of primates and carnivores where a functional organization for this selectivity is also observed: neurons are organized in a columnar fashion with shared orientation preference across cortical layers and smooth changes in selectivity along the V1 surface (Hubel and Wiesel, 1977). This functional architecture is the product of the spatial arrangement of ON and OFF thalamocortical inputs that innervate V1 (Kremkow et al., 2016; Lee et al., 2016a) and of the vertical bias of intracortical connectivity (Song et al., 2005). These spatially offset ON and OFF afferents converge on individual V1 neurons to generate receptive fields that are orientation tuned (Alonso et al., 2001) and well described by Gabor functions (Jones and Palmer, 1987) (Figure 1A).

Such a functional architecture for orientation selectivity, however, is not common to all mammals: V1 of rodents and lagomorphs lack it, but their neurons are still orientation selective (Dräger, 1975; Girman et al., 1999; Métin et al., 1988; Murphy and Berman, 1979; Van Hooser et al., 2005). This raises the question of what connectivity rules guide afferent and intracortical circuitry to generate orientation selectivity in mammals that lack a functional architecture for orientation selectivity (Ohki and Reid, 2007).

We recently showed in a model of rodent V1 that layer 2/3 (L2/3) can inherit orientation selectivity from orientation selective neurons in layer 4 (L4) even if recurrent as well as feedforward (L4 to L2/3) connectivity is random (Hansel and van Vreeswijk, 2012). In this model, the L2/3 network operates in a ''balanced'' regime (van Vreeswijk and Sompolinsky, 1996, 1998), in which excitatory and inhibitory inputs are both strong and roughly cancel each other (Hansel and van Vreeswijk, 2012; Pehlevan and Sompolinsky, 2014).

In this report, we address the question of whether orientation selectivity can emerge in rodent V1 from random connectivity. We present a strongly recurrent model of the rodent V1 network in which neurons receive inputs from randomly chosen non-selective lateral geniculate nucleus (LGN) cells. The model does not necessitate sparse connectivity to generate selectivity, as is required in previous random network-based models of orientation tuning (Ringach, 2004; Soodak, 1987; von der Malsburg, 1973). Remarkably, orientation selectivity emerges in this network despite the lack of a Gabor-like structure of the thalamocortical input with well-segregated ON and OFF subfields. Furthermore, orientation selectivity in this network is robust to changes in the number of inputs. A key prediction of this model is that the orientation selectivity of V1 neurons may vary with the spatial content of the presented stimulus (Miller, 2016). It thus predicts that in mouse V1 receptive fields in the frequency domain are intricate, containing dependencies between orientation and spatial frequency, in stark contrast to observations made in primates and carnivores, and predictions of Gabor receptive fields (De Valois et al., 1982; Jones et al., 1987; Webster and De Valois, 1985). To test these predictions, we quantified in mouse V1 the degree to which orientation preference is linked to the stimulus spatial frequency using a

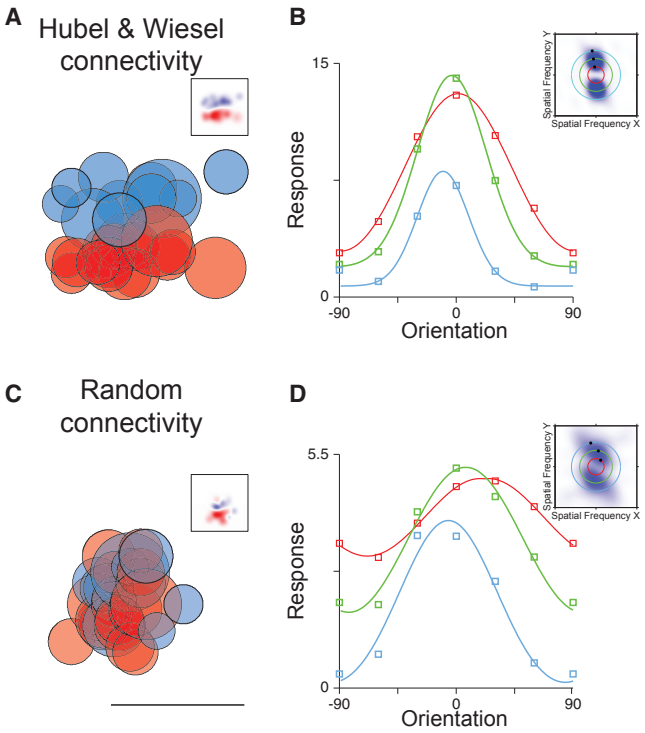

Figure 1. Receptive Fields, Random Connectivity, Spatial Frequency (SF) Tuning, and Orientation Tuning

(A) Hubel and Wiesel connectivity in which ON (red) and OFF (blue) thalamocortical afferents, with spatial receptive fields indicated by each circle, converge onto a neuron in primary visual cortex. The summation of these afferent receptive fields generates a Gabor-like receptive field in visual cortex (inset).

(B) Orientation preference does not change with SF for such receptive fields. Tuning curves of the temporal modulation of the response for low (red), medium (green), and high (blue) spatial frequencies are plotted. In frequency space, these receptive fields maintain a peak response at a consistent angle that points toward the origin at the midpoint of the graph (inset).

(C) Random connectivity from the lateral geniculate nucleus (LGN) in which ON and OFF thalamocortical neurons with similar spatial receptive fields converge on cortical neurons also generates orientation selectivity in the temporal modulation of the response. The linear summation of LGN ON and OFF neuron receptive fields shows oriented profiles (inset). Scale bar indicates 35 degrees.

(D) Orientation preference shifts for random connectivity as SF changes. Orientation tuning curves are plotted as in (B). In frequency space, these receptive fields tilt in a manner that does not project back to the origin.

combination of electrophysiological and imaging measurements. In agreement with our model, we found that orientation preference depends on spatial frequency for some V1 neurons.

RESULTS

To contrast different circuitry that could give rise to cortical orientation selectivity, we constructed two model V1 neurons that receive input from the thalamus. In one model, the V1 neuron receives ON and OFF thalamic inputs that are sampled on the basis of a Gabor filter: ON and OFF inputs have spatial preferences elongated along the preferred orientation axis and are spatially segregated (Figure 1A). The temporally modulated component (F1) of the response is largest to horizontally oriented drifting gratings regardless of the spatial frequency (Figure 1B). We also constructed a model V1 neuron that receives ON and OFF inputs with nearby spatial preferences (dispersion SD, 7 degrees), which are randomly intermixed (Figure 1C). Remarkably, this random connectivity model also exhibits orientation selectivity in the F1 component of the response. It emerges from the imbalances in ON and OFF inputs onto the target neuron. Unlike the ordered receptive field neuron, however, the preferred orientation of the F1 response of the cell changes with the stimulus spatial frequency. At high spatial frequency, the F1 responses of the model neuron are largest for stimuli oriented at 30 degrees, while at low spatial frequency responses are largest at −10 degrees (Figure 1D). This shift in orientation preference is a product of the random connectivity onto the neuron: the imbalances of ON and OFF thalamic inputs are different as spatial scale changes, causing shifts in orientation preference.

Orientation Selectivity Emerges in a Model of Rodent V1 with Random Wiring

To study whether orientation selectivity in mouse V1 could result from random connectivity, we constructed a large-scale conductance-based spiking network model of V1 (Figure S1) in which cortical neurons receive feedforward excitation from randomly chosen thalamic relay cells as well as other cortical cells of similar retinotopic preferences (Figure S1B; see STAR Methods). Previously it has been shown that orientation selectivity can emerge on the basis of random inputs alone (Ringach, 2004; Soodak, 1987; von der Malsburg, 1973). Orientation selectivity arises in these models because of asymmetries in the spatial preferences of the sparse inputs that converge onto a cortical neuron. As the number of convergent inputs increases, however, the selectivity declines because the tuned temporally modulated component of the LGN input decreases relative to the time-averaged untuned component. To surmount this dependence of orientation selectivity on the number of inputs, we employ a network model in which excitatory and inhibitory inputs are strong but balanced (van Vreeswijk and Sompolinsky, 1996, 1998) such that the mean and variance of the net input is on the order of the distance to threshold (Figure S1E).

Networks with random connectivity operating in a balanced regime have previously been shown to *maintain* preferences present in the input (Hansel and van Vreeswijk, 2012). We hypothesized that orientation selectivity would emerge in our model if the spatial inhomogeneity in the aggregate thalamic input were maintained in the output by the balance of excitation and inhibition. In the balanced state, the untuned time-averaged component of the input is largely suppressed by the intracortical feedback, leading to a net input in which the tuned modulation is comparable to the untuned component. Indeed, orientation selectivity emerges in our model (Figure 2A), varying between highly selective neurons (e.g., model neuron E10371) to weakly selective (e.g., model neuron E11763). This diversity of selectivity results in a distribution of orientation selectivity index (OSI) demonstrating that orientation selectivity emerges naturally in a random connectivity model (Figures 2, S1F, S2, and S3). The emergent cortical orientation preference is matched to the

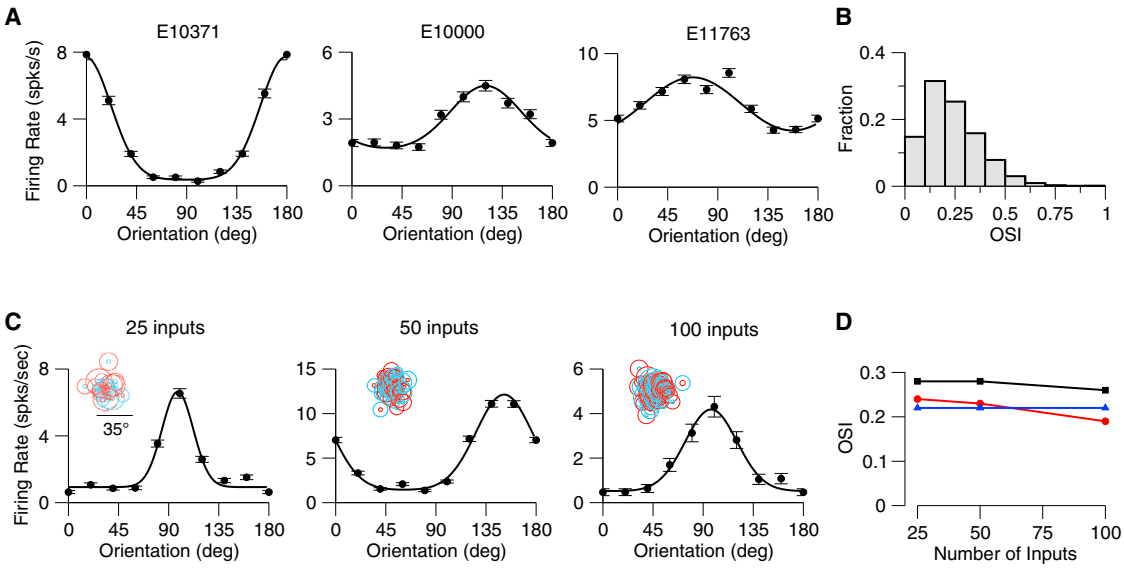

Figure 2. Orientation Selectivity Emerges in the Mouse V1 Model

(A) Examples of tuning curves (peak firing rate) of three excitatory V1 neurons in the model. SF of the drifting grating is 0.03 cyc/deg. OSIs from left to right are as follows: 0.62, 0.23, and 0.15. Error bars represent the SEM.

(B) Distribution of OSI (peak response) over all the neurons (neurons in the central part of the network; see STAR Methods; n = 5,041). Mean OSI = 0.24 (mean OSIs of the F0 and F1 components of the response are 0.29 and 0.19).

(C) Examples of tuning curves of excitatory neurons in networks with different average number of thalamic inputs per neuron. From left to right: OSI = 0.47, 0.48, and 0.49.

(D) Population average OSIs versus average number of thalamic inputs. Red: Peak spike response. Black: F1 component of the spike response. Blue: F1 component of the thalamic excitatory input.

preferred orientation of aggregate thalamic input (Figures S2A and S2B), as observed in mouse visual cortex (Li et al., 2013). In this balanced model, the emergent orientation selectivity should be insensitive to the number of inputs. To verify this, we varied this number from 25 to 100 and found that the degree of orientation selectivity was maintained (Figures 2C, 2D, and S3). The emergent selectivity is also robust to changes in network size and in synaptic strength (Figures S3A and S3B).

Orientation selectivity emerges in our random connectivity model because of the spatial inhomogeneity in inputs to cortical neurons. In particular, the convergence of ON and OFF thalamic inputs onto model neurons are spatially offset from one another. The orientation of this offset may be related to the emergent orientation preference of neurons (Lien and Scanziani, 2013; Liu et al., 2010). To assess this relationship, we estimated the ON and OFF subfields of the thalamic inputs by presenting spots at different locations to the model network as in Lien and Scanziani (2013) (see STAR Methods). The estimated ON and OFF subfields for four example neurons reveal different offsets. When ON and OFF subfields have large horizontal displacements (E14493, E14847) preference for the vertical orientation of the drifting grating at 0.03 cyc/deg tends to emerge, whereas when ON and OFF subfields are vertically displaced preference for horizontal orientations tends to emerge (Figure 3A, E14664). The offsets in ON and OFF subfields that emerge from the random connectivity model (Figure 3B) are similar to those observed experimentally (Lien and Scanziani, 2013). When the ON/OFF offset is large, there is a strong correspondence between the axis of the offset and the preferred orientation of the thalamic input (Figure 3). The ON and OFF displacement, however, is not the only factor that contributes to this orientation preference. The randomness in the feedforward connectivity generates ON and OFF subfields of the thalamic excitation that deviate from circularity. The shape of the subfields, and the interaction between the subfields, can create orientation preferences that deviate from that predicted from the offset of ON and OFF subfields (Figure 3A, example 15022). In sum, the offset of ON and OFF subfields, their interaction, and their shape influence the emergent thalamic orientation selectivity. Because the thalamic input selectivity is directly related to the cortical output selectivity (Figures S2A and S2B), these factors impact the emergent cortical orientation selectivity in the same way. The emergent orientation preference, however, is particularly sensitive to the spatial structure of the stimulus (Figure 1).

Dependence of Preferred Orientation on Spatial Frequency in the Model

We then characterized how much the properties of the neuronal responses vary with spatial frequency in the model. First, we investigated how the population average peak response and OSI were affected when changing spatial frequency (SF). We found that, although the mean population response was modulated by SF (maximal response for SF, 0.035 cyc/deg), the overall selectivity of the population was less sensitive to SF (Figures S2D and S2E). This mild effect across the population contrasts with the effect of SF changes on the preferred orientation of individual

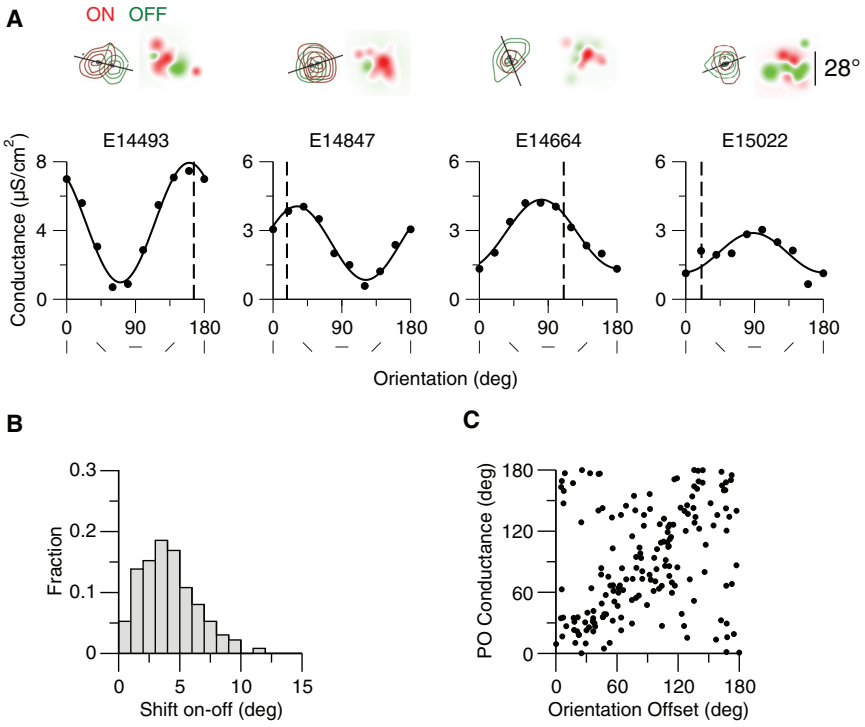

Figure 3. The Contribution of the Offset of ON and OFF Subregions of the Thalamic Excitation to Its Orientation Preference

The ON and OFF subfields of the thalamic inputs were estimated by presenting spots at different locations to the model network as in Lien and Scanziani (2013) (see STAR Methods).

(A) Top panels: ON (red) and OFF (green) subfields of the thalamic excitation for four example neurons. Dark spots: Center of mass of the subfields. The solid line indicates the axis of the offset of the two centers of mass. Receptive fields based on the summed ON and OFF thalamic inputs are shown on the right. The scale bar on the right applies to all receptive fields. Bottom panels: Tuning curves of the thalamic excitation for these neurons. The SF of the drifting grating is 0.03 cyc/deg. Vertical dashed line indicates the orientation of the offset axis (0° corresponds to an horizontal axis). Offset amplitude and orientation and preference of the thalamic excitation are as follows: E14493, 11.4°, 166.1°, 160.3°; E14847, 4.7°, 18.2°, 31.1°; E14664, 3.9°, 111.4°, 80.7°; E15022, 2.8°, 20.6°, 88.0°.

(B) Offset distribution across neurons (n = 361; neurons are at the center of the network, see STAR Methods). Mean offset: 4.1°.

(C) Orientation preference of the thalamic input conductance (drifting grating with 0.03 cyc/deg) versus orientation from the offset axis (perpendicular to the offset axis) for all neurons with an offset larger than 4° (n = 170). The CC is 0.24.

neurons. As we varied SF, the preferred orientation of neurons often changed (top and bottom left panels in Figure 4A; Figures 4B and 4C, pink). We quantified this change by computing the circular correlation (CC, see STAR Methods) of the preferred orientation at different spatial frequencies across neurons. This correlation was strong for nearby spatial frequencies, whereas for spatial frequencies far apart it was weaker (Figures 4B and 4C). It declined from 0.71 for 0.04–0.03 cyc/deg to 0.00 for 0.04–0.01 cyc/deg (Figure 5, ΔCC = 0.71). We found that this effect was robust to changes in the network size, the number of connections per neuron, and the synaptic conductance strengths (Figure S3). We also found that it was qualitatively robust to changes in the spatial dispersion of the thalamic feedforward connections but that the decorrelation was weaker for smaller dispersions (Figures S3C and S3D).

Dependence of Preferred Orientation on SF in Mouse V1

These theoretical results prompted us to determine whether SF has a similar effect on orientation preference in mouse V1. Varying SF yielded shifts in orientation preference for many, but not all, neurons when measured using intracellular, whole-cell, recordings (Figure 4A, middle: top and bottom panels; Figure 4C, blue panels). Changes in orientation preference were observed both at the level of spike rate and membrane potential (38 total cells; Figure S4). To gain access to this effect in large populations of V1 neurons, we also examined it by measuring calcium responses using two-photon microscopy (606 total cells; Figure 4A, left: top and bottom panels; Figures 4B and 4C, green panels; Figure S5). As with our electrophysiological data, we found a diversity of changes with SF: preference shifted dramatically for some neurons and not for others.

These differences in preferred orientation observed from our Ca^{2+} responses could be due to noise in our measurements. To be included in our population analysis, cells were required to have a minimum peak response of 8% at both frequencies. Using different thresholds to include cells yields similar declines in correlation when comparing orientation preference at 0.04 cyc/deg to 0.03 and 0.01 cyc/deg (8%: ΔCC = 0.46 with 90 cells for 0.01 and 0.04 cyc/deg and 288 cells for 0.03 and 0.04 cyc/deg; 10%: ΔCC = 0.4 with 43 cells for 0.01 and 0.04 cyc/deg and 182 cells for 0.03 and 0.04 cyc/deg; 12%: ΔCC = 0.52 with 22 cells for 0.01 and 0.04 cyc/deg and 139 cells for 0.03 and 0.04 cyc/deg). To address whether the observed effect was influenced by differences in response amplitude for different spatial frequencies, we also restricted our analysis to neurons with differences in peak response amplitudes less than 10% (Figure S6). This also did not alter the decline in CC (ΔCC = 0.49, n = 86 for 0.01 and 0.04 cyc/deg and n = 259 for 0.03 and 0.04 cyc/deg). Furthermore, we examined whether the reduction in CC was related to the OSI of neurons by restricting our analysis to only those cells within the top 25% of our distribution. This restriction yields a similar ΔCC of 0.45 (n = 23, 0.01–0.04 comparison, n = 72 for 0.03–0.04 comparison). In sum, orientation preference changed with SF in electrophysiology records as well as calcium imaging measurements.

We have found that both the model and actual mouse V1 neurons exhibit changes in orientation preference with SF in a similar fashion (Figure 5). That is, for small-frequency shifts, the model

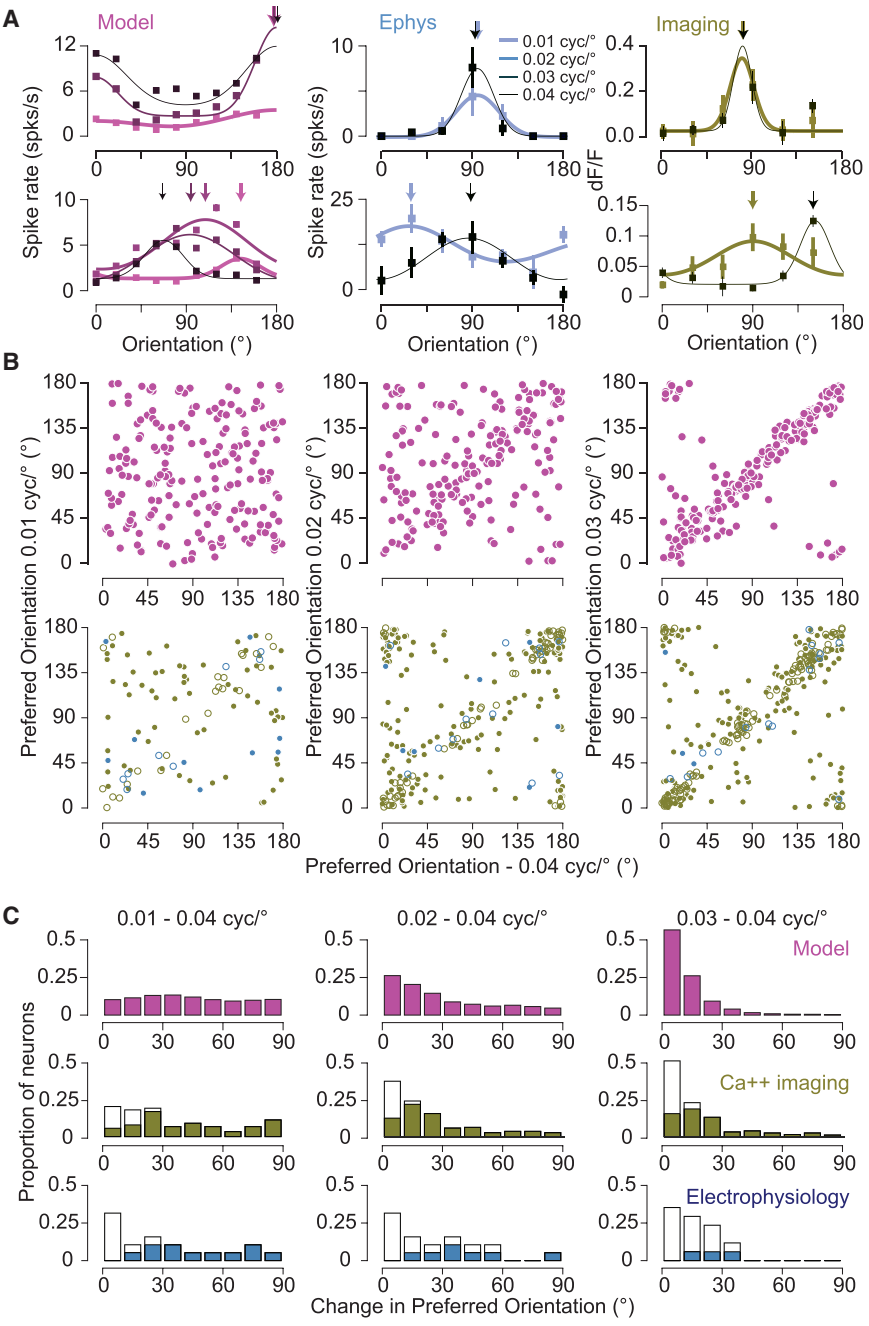

Figure 4. SF and Orientation Selectivity in the Model and Mouse V1

(A) Example orientation tuning curves based on spike rate are plotted for neurons in the spiking network model (left), electrophysiology (middle), and based on fluorescence changes from calcium imaging experiments (right). Orientation tuning curves are plotted for different spatial frequencies, from 0.01 to 0.04 cyc/deg, indicated by line thickness. If the error bars are not visible, they are smaller than the symbol size. Error bars represent SEM.

(B) Top row: The relationship between preferred orientation in the model. Left: 0.04 cyc/deg and 0.01 cyc/deg. Middle: 0.04 cyc/deg and 0.02 cyc/deg. Right: 0.04 cyc/deg and 0.03 cyc/deg. Bottom row: The same for the calcium and electrophysiological records (green and blue symbols, respectively). The bootstrapped vector average is used as the estimate of the preferred orientation. For calcium and spiking data, statistically significant shifts in orientation preference are indicated by filled circles. Number of cells in the imaging data for comparison of 0.01 and 0.04 cyc/deg is 90, for comparison of 0.02 and 0.04 cyc/deg is 228, and for comparison of 0.03 and 0.04 cyc/deg is 288. Number of cells in the electrophysiological data for comparison of 0.01 and 0.04 cyc/deg is 19, for comparison of 0.02 and 0.04 cyc/deg is 19, and for comparison of 0.03 and 0.04 cyc/deg is 17.

(C) Histograms of the difference in orientation preference between 0.04 cyc/deg and 0.01 (left), 0.02 (middle), and 0.03 (right) cyc/deg. Filled bars for electrophysiology and calcium imaging data indicate statistically significant changes in orientation preference.

and actual neurons have similar orientation preferences, as indicated by a high CC, whereas large changes in SF cause substantial decreases in CC. One notable discrepancy between the model and actual data is that nearby spatial frequencies have higher correlations for the model than for the data. A factor that contributes to this discrepancy is the amount of data collected in the model records relative to the physiological records (between 10 and 24 s for each orientation and SF). When we limit the records from which the model data are based to 20 s, instead of 80 s, ΔCC declines from 0.71 to 0.58. An additional factor we considered is the nature of the thalamocortical input. Orientation selectivity does exist in mouse thalamic neurons (Piscopo et al., 2013; Scholl et al., 2013; Zhao et al., 2013), so we also explored the impact of elongated thalamic receptive fields on the properties of the cortical model (Figure S7). This impact was modest, slightly altering the dependence of orientation preference on SF (Figure 5, elongated thalamic receptive field model, ΔCC = 0.73; Figures S7F and S7G), while increasing the overall orientation selectivity of V1 excitatory neurons (mean OSI = 0.32 versus 0.23 for circular thalamic receptive field; Figure S7B).

Two-Dimensional SF Filters of Neurons in Mouse V1 Are Non-separable

The observed dependence of orientation preference on SF for some V1 neurons indicates that these neurons' receptive fields are not simple orientation detectors. Instead, they may be measuring components of the visual scene that are better characterized by a conjunction of two-dimensional SF filters. We therefore measured responses of V1 neurons while varying

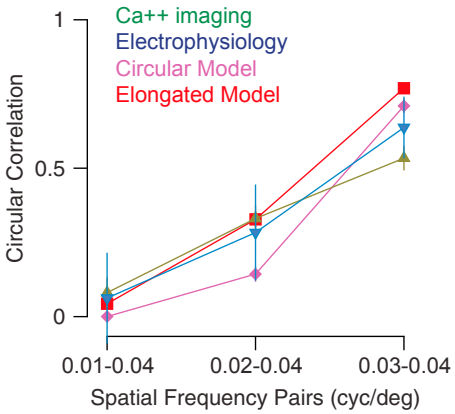

Figure 5. Comparison between Model and Experimental Results

Graph indicates the observed CC between preferred orientations of single neurons at two spatial frequencies. The pairs of spatial frequencies being compared are indicated on the x axis. Green: Calcium imaging. Blue: Electrophysiology. Purple: Model with circular thalamic receptive fields (same as in Figure 4). Red: Model with elongated thalamic receptive fields (see Results and Figure S9). Error bars are bootstrapped 95% confidence intervals on the CC. For calcium: CC for 0.01–0.04 cyc/deg = 0.08, for 0.02–0.04 cyc/deg = 0.33, and for 0.03–0.04 cyc/deg = 0.53. Electrophysiological data: CC for 0.01–0.04 cyc/deg = 0.03, for 0.02–0.04 cyc/deg = 0.28, and for 0.03–0.04 cyc/deg = 0.67.

vertical and horizontal SF components (Ringach et al., 2016) (24 cells, Hartley gratings; see STAR Methods; Figure 6A). Neurons whose orientation selectivity is invariant to SF, would exhibit preference profiles for which angle (orientation) does not change with the distance from the origin (SF). As before, different neurons revealed a diversity of behaviors (similar to kernels shown in Ringach et al., 2016), from invariance (Figure 6A, left) to systematic change in selectivity with SF (Figure 6A, middle). We also recorded from a small number of inhibitory neurons (identified based on spike rate and action potential width) with broad selectivity for orientation and SF (Niell and Stryker, 2008) (Figure 6A, right). Measures of orientation preference based on the Hartley stimulus qualitatively agree with those made by measuring orientation tuning curves at different spatial frequencies (compare top and bottom panels in Figure 6A). This indicates that many V1 neurons are better characterized as containing receptive fields that are a conjunction of horizontal and vertical SF filters instead of invariant selectivity for orientation. We performed a comparable analysis in our V1 network model (see STAR Methods) and found a similar behavior (Figures 6B and S8).

DISCUSSION

We have presented a network model for rodent V1 that demonstrates that orientation selectivity can emerge from random connectivity even if LGN cells are not selective. It makes the specific prediction that this selectivity should be sensitive to spatial form for some V1 neurons. Testing that prediction in mouse visual cortex, we found a similar effect. Using a model that receives thalamic inputs that exhibited some orientation selectivity increased the degree of cortical orientation selectivity yielding distributions of OSI closer to experimental estimates. This model also exhibited a similar dependence of orientation preference on SF.

In our models, there is a strong overlap of the ON and OFF subregions of the thalamic inputs as seen in experiments (Li et al., 2013; Lien and Scanziani, 2013; Liu et al., 2010). When the offset between the centers of the ON and OFF subfields is large, the orientation of this offset can be predictive of the orientation preference of the neuronal response. Nevertheless, even when this offset is large, the orientation preference can change substantially with SF. In our model, the orientation of the offset and the orientation preference of the neuronal response are strongly correlated for intermediate SF only (Figure S9).

Quantitatively, the decorrelation of preferred orientation with SF is somewhat weaker in experiments when compared to our models. One source of this discrepancy is related to the amount of data collected for the model and the experiments. When records for the model are limited to 20 s, the model ΔCC was 0.59, close to the experimental value of ΔCC = 0.46. The change in ΔCC is due to the decline in CC between 0.03 to 0.04 cyc/deg from 0.71 to 0.59. Another possible source for this difference is that we did not incorporate any feature-specific component in the connectivity even though this has been shown to be present in mouse V1 after the critical period (Ko et al., 2011, 2013; Lee et al., 2016b).

We have demonstrated that V1 neurons' receptive fields are surprisingly intricate (Figures 6 and S8). This complexity stands in contrast to the V1 receptive fields in cats (Hammond and Pomfrett, 1990; Jones et al., 1987; Webster and De Valois, 1985) and primates (De Valois et al., 1982), where orientation preference is represented in a separable manner from spatial form. A similar dependence in the mouse V1 was reported in a study based on calcium imaging (Ayzenshtat et al., 2016). There, it was demonstrated that a reduction in SF by one octave causes a mean shift in preferred orientation by 22.1°, comparable to our own estimates of the change in orientation when shifting from 0.04 to 0.02 cyc/deg (model, mean ΔPO = 29.8°; ephys, ΔPO = 30.2°; Ca^{2+}, ΔPO = 22.2°). They proposed that the dependence could arise from separable selectivity in frequency domain. We demonstrate here that while some V1 neurons do have separable frequency domain receptive fields, V1 receptive fields exhibit diverse dependencies that yield SF-invariant orientation preferences (Figure 6, first column) or SF-dependent orientation preferences (Figure 6, second column).

Such receptive field complexity likely has an impact on connectivity patterns within V1. In primates and carnivores where preferred orientations are similar for different spatial frequencies, neurons with similar orientation preferences are much more likely to be connected (Bosking et al., 1997; Wilson et al., 2016). In mice, neurons with similar orientation preference have been reported to be somewhat more likely to be connected (Ko et al., 2011, 2013). However, in these experiments, difference in preferred orientation was measured at only one SF (0.045 cyc/deg). As we have shown, this difference varies with SF and the connectivity is likely to depend on the similarity in response at all spatial frequencies. Indeed, correlation in the response to natural stimuli was found to be a stronger factor than orientation preference at one SF in determining connection probability (Cossell et al., 2015; Ko et al., 2013).

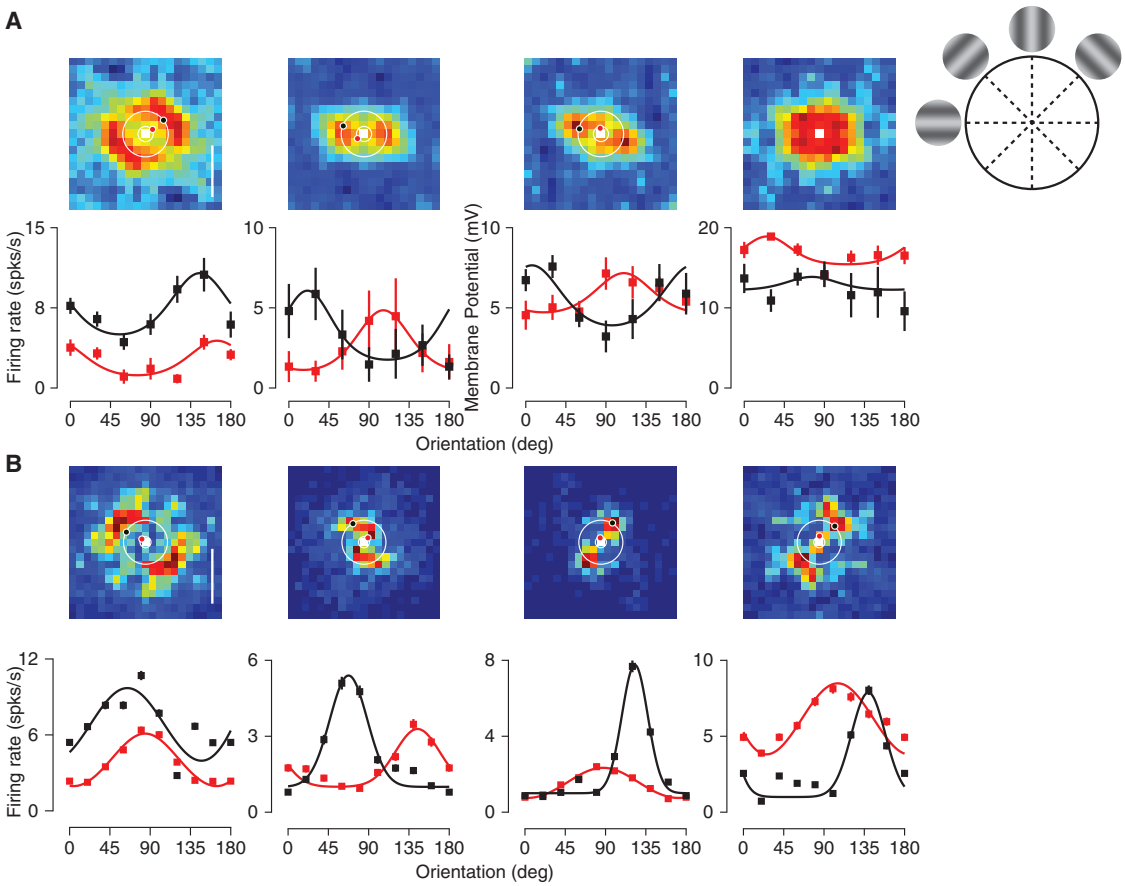

Figure 6. Neuron Receptive Fields in the Frequency Domain Are Intricate

(A) Mean membrane potential responses to Hartley stimuli (see STAR Methods) are plotted for combinations of horizontal and vertical spatial frequencies (top row). Circles indicate stimulus combinations corresponding to oriented gratings at fixed spatial frequencies. The red and black dots indicate the peak response at those spatial frequencies. Each panel corresponds to a different example cell. Orientation tuning curves for drifting gratings at 0.014 cyc/deg (red) and 0.044 cyc/deg (black) are shown for these four neurons (bottom row). Error bars represent SEM.

(B) Example frequency receptive fields for four neurons in the model. Orientation tuning curves at 0.01 cyc/deg (red) and 0.04 cyc/deg (black) are shown for these neurons (bottom row) based on responses to drifting gratings.

The intricate receptive field profiles described here are akin to those observed in primary auditory cortex. Auditory cortex neurons are sensitive to the combination of many auditory cues (Wang et al., 2005), which may comprise a synthesis sufficient to detect auditory objects (Bar-Yosef and Nelken, 2007). The frequency domain receptive field profiles observed in mouse V1 neurons may therefore reflect a similar progression toward a representation for objects using a random connectivity scheme that occurs as information flows through the visual pathway.

To conclude, our investigation demonstrates that random connectivity can be the dominant component accounting for emergent properties such as orientation selectivity. An important advantage of random wiring schemes is that they occur naturally, following the broader patterns of retinotopy that are formed by biochemical gradients. This natural emergence may thus reflect a wiring strategy that allows for selectivity without the cost associated with constructing specific afferent wiring connections.

STAR★METHODS

Detailed methods are provided in the online version of this paper and include the following:

- KEY RESOURCES TABLE
- CONTACT FOR REAGENT AND RESOURCE SHARING
- EXPERIMENTAL MODEL AND SUBJECT DETAILS
  - Mice
- METHOD DETAILS
  - Detailed Experimental Methods
  - Detailed Computational Model of Mouse V1
- QUANTIFICATION AND STATISTICAL ANALYSIS
  - Experimental Analysis
  - Model Analysis

SUPPLEMENTAL INFORMATION

Supplemental Information includes nine figures and three tables can be found with this article online at https://doi.org/10.1016/j.celrep.2018.07.054.

ACKNOWLEDGMENTS

We are grateful to Ran Darshan, Carole Levenes, and Gianluigi Mongillo for helpful discussions and comments and Baowang Li for conducting some of the electrophysiology experiments. This work was supported by a CRCNS grant; ANR Grant 14-NEUC-0001-01; NIH Grant EY-020592; ANR Grant 13-BSV4-0014-02 (C.v.V. and D.H.); and CONICET Grant PIP 112 201301 00256 (G.M.). Part of the modeling work was performed in the framework of the France-Israel Laboratory of Neuroscience (D.H. and C.v.V.). J.J.P. is a Howard Hughes Medical Institute International Student Research Fellow.

AUTHOR CONTRIBUTIONS

Conceptualization, J.J.P., G.M., C.v.V., N.J.P., and D.H.; Methodology, G.M., C.v.V., and D.H.; Investigation, J.J.P. and N.J.P.; Formal Analysis, J.J.P. and N.J.P.; Writing – Original Draft, J.J.P., G.M., C.v.V., N.J.P., and D.H.; Writing – Review and Editing, J.J.P., G.M., C.v.V., N.J.P., and D.H.; Funding Acquisition, C.v.V., N.J.P., and D.H.

DECLARATION OF INTERESTS

The authors declare no competing interests.

Received: July 17, 2017
Revised: May 25, 2018
Accepted: July 16, 2018
Published: August 21, 2018

REFERENCES

Alonso, J.M., Usrey, W.M., and Reid, R.C. (2001). Rules of connectivity between geniculate cells and simple cells in cat primary visual cortex. J. Neurosci. *21*, 4002–4015.

Ayzenshtat, I., Jackson, J., and Yuste, R. (2016). Orientation tuning depends on spatial frequency in mouse visual cortex. eNeuro *3*, ENEURO.0217-16.2016.

Bar-Yosef, O., and Nelken, I. (2007). The effects of background noise on the neural responses to natural sounds in cat primary auditory cortex. Front. Comput. Neurosci. *1*, 3.

Bosking, W.H., Zhang, Y., Schofield, B., and Fitzpatrick, D. (1997). Orientation selectivity and the arrangement of horizontal connections in tree shrew striate cortex. J. Neurosci. *17*, 2112–2127.

Brainard, D.H. (1997). The Psychophysics Toolbox. Spat. Vis. *10*, 433–436.

Carandini, M., and Ferster, D. (2000). Membrane potential and firing rate in cat primary visual cortex. J. Neurosci. *20*, 470–484.

Cossell, L., Iacaruso, M.F., Muir, D.R., Houlton, R., Sader, E.N., Ko, H., Hofer, S.B., and Mrsic-Flogel, T.D. (2015). Functional organization of excitatory synaptic strength in primary visual cortex. Nature *518*, 399–403.

De Valois, R.L., Albrecht, D.G., and Thorell, L.G. (1982). Spatial frequency selectivity of cells in macaque visual cortex. Vision Res. *22*, 545–559.

Dräger, U.C. (1975). Receptive fields of single cells and topography in mouse visual cortex. J. Comp. Neurol. *160*, 269–290.

Girman, S.V., Sauvé, Y., and Lund, R.D. (1999). Receptive field properties of single neurons in rat primary visual cortex. J. Neurophysiol. *82*, 301–311.

Golshani, P., and Portera-Cailliau, C. (2008). In vivo 2-photon calcium imaging in layer 2/3 of mice. J. Vis. Exp. *2008*, 681.

Hammond, P., and Pomfrett, C.J. (1990). Influence of spatial frequency on tuning and bias for orientation and direction in the cat's striate cortex. Vision Res. *30*, 359–369.

Hansel, D., and van Vreeswijk, C. (2012). The mechanism of orientation selectivity in primary visual cortex without a functional map. J. Neurosci. *32*, 4049–4064.

Hubel, D.H., and Wiesel, T.N. (1962). Receptive fields, binocular interaction and functional architecture in the cat's visual cortex. J. Physiol. *160*, 106–154.

Hubel, D.H., and Wiesel, T.N. (1977). Ferrier lecture. Functional architecture of macaque visual cortex. Proc. R. Soc. Lond. B Biol. Sci. *198*, 1–59.

Jones, J.P., and Palmer, L.A. (1987). The two-dimensional spatial structure of simple receptive fields in cat striate cortex. J. Neurophysiol. *58*, 1187–1211.

Jones, J.P., Stepnoski, A., and Palmer, L.A. (1987). The two-dimensional spectral structure of simple receptive fields in cat striate cortex. J. Neurophysiol. *58*, 1212–1232.

Kalatsky, V.A., and Stryker, M.P. (2003). New paradigm for optical imaging: temporally encoded maps of intrinsic signal. Neuron *38*, 529–545.

Kerr, J.N., Greenberg, D., and Helmchen, F. (2005). Imaging input and output of neocortical networks in vivo. Proc. Natl. Acad. Sci. USA *102*, 14063–14068.

Ko, H., Hofer, S.B., Pichler, B., Buchanan, K.A., Sjöström, P.J., and Mrsic-Flogel, T.D. (2011). Functional specificity of local synaptic connections in neocortical networks. Nature *473*, 87–91.

Ko, H., Cossell, L., Baragli, C., Antolik, J., Clopath, C., Hofer, S.B., and Mrsic-Flogel, T.D. (2013). The emergence of functional microcircuits in visual cortex. Nature *496*, 96–100.

Kremkow, J., Jin, J., Wang, Y., and Alonso, J.M. (2016). Principles underlying sensory map topography in primary visual cortex. Nature *533*, 52–57.

Lee, K.S., Huang, X., and Fitzpatrick, D. (2016a). Topology of ON and OFF inputs in visual cortex enables an invariant columnar architecture. Nature *533*, 90–94.

Lee, W.C., Bonin, V., Reed, M., Graham, B.J., Hood, G., Glattfelder, K., and Reid, R.C. (2016b). Anatomy and function of an excitatory network in the visual cortex. Nature *532*, 370–374.

Li, Y.T., Ibrahim, L.A., Liu, B.H., Zhang, L.I., and Tao, H.W. (2013). Linear transformation of thalamocortical input by intracortical excitation. Nat. Neurosci. *16*, 1324–1330.

Lien, A.D., and Scanziani, M. (2013). Tuned thalamic excitation is amplified by visual cortical circuits. Nat. Neurosci. *16*, 1315–1323.

Liu, B.H., Li, P., Sun, Y.J., Li, Y.T., Zhang, L.I., and Tao, H.W. (2010). Intervening inhibition underlies simple-cell receptive field structure in visual cortex. Nat. Neurosci. *13*, 89–96.

Malone, B.J., and Ringach, D.L. (2008). Dynamics of tuning in the Fourier domain. J. Neurophysiol. *100*, 239–248.

Métin, C., Godement, P., and Imbert, M. (1988). The primary visual cortex in the mouse: receptive field properties and functional organization. Exp. Brain Res. *69*, 594–612.

Miller, K.D. (2016). Canonical computations of cerebral cortex. Curr. Opin. Neurobiol. *37*, 75–84.

Mrsic-Flogel, T.D., Hofer, S.B., Ohki, K., Reid, R.C., Bonhoeffer, T., and Hübener, M. (2007). Homeostatic regulation of eye-specific responses in visual cortex during ocular dominance plasticity. Neuron *54*, 961–972.

Murphy, E.H., and Berman, N. (1979). The rabbit and the cat: a comparison of some features of response properties of single cells in the primary visual cortex. J. Comp. Neurol. *188*, 401–427.

Nauhaus, I., Nielsen, K.J., and Callaway, E.M. (2012). Nonlinearity of two-photon Ca^{2+} imaging yields distorted measurements of tuning for V1 neuronal populations. J. Neurophysiol. *107*, 923–936.

Niell, C.M., and Stryker, M.P. (2008). Highly selective receptive fields in mouse visual cortex. J. Neurosci. *28*, 7520–7536.

Ohki, K., and Reid, R.C. (2007). Specificity and randomness in the visual cortex. Curr. Opin. Neurobiol. *17*, 401–407.

Ohki, K., Chung, S., Ch'ng, Y.H., Kara, P., and Reid, R.C. (2005). Functional imaging with cellular resolution reveals precise micro-architecture in visual cortex. Nature *433*, 597–603.

Pehlevan, C., and Sompolinsky, H. (2014). Selectivity and sparseness in randomly connected balanced networks. PLoS One *9*, e89992.

Pelli, D.G. (1997). The VideoToolbox software for visual psychophysics: transforming numbers into movies. Spat. Vis. *10*, 437–442.

Piscopo, D.M., El-Danaf, R.N., Huberman, A.D., and Niell, C.M. (2013). Diverse visual features encoded in mouse lateral geniculate nucleus. J. Neurosci. *33*, 4642–4656.

Press, W.H. (1992). Numerical Recipes in C: The Art of Scientific Computing, Second Edition (Cambridge University Press).

Priebe, N.J., and Ferster, D. (2012). Mechanisms of neuronal computation in mammalian visual cortex. Neuron *75*, 194–208.

Reyes, A., and Sakmann, B. (1999). Developmental switch in the short-term modification of unitary EPSPs evoked in layer 2/3 and layer 5 pyramidal neurons of rat neocortex. J. Neurosci. *19*, 3827–3835.

Ringach, D.L. (2004). Haphazard wiring of simple receptive fields and orientation columns in visual cortex. J. Neurophysiol. *92*, 468–476.

Ringach, D.L., Shapley, R.M., and Hawken, M.J. (2002). Orientation selectivity in macaque V1: diversity and laminar dependence. J. Neurosci. *22*, 5639–5651.

Ringach, D.L., Mineault, P.J., Tring, E., Olivas, N.D., Garcia-Junco-Clemente, P., and Trachtenberg, J.T. (2016). Spatial clustering of tuning in mouse primary visual cortex. Nat. Commun. *7*, 12270.

Sarnaik, R., Chen, H., Liu, X., and Cang, J. (2014). Genetic disruption of the On visual pathway affects cortical orientation selectivity and contrast sensitivity in mice. J. Neurophysiol. *111*, 2276–2286.

Scholl, B., Tan, A.Y., Corey, J., and Priebe, N.J. (2013). Emergence of orientation selectivity in the Mammalian visual pathway. J. Neurosci. *33*, 10616–10624.

Scholl, B., Pattadkal, J.J., Dilly, G.A., Priebe, N.J., and Zemelman, B.V. (2015). Local integration accounts for weak selectivity of mouse neocortical parvalbumin interneurons. Neuron *87*, 424–436.

Scholl, B., Pattadkal, J.J., Rowe, A., and Priebe, N.J. (2017). Functional characterization and spatial clustering of visual cortical neurons in the predatory grasshopper mouse *Onychomys arenicola*. J. Neurophysiol. *117*, 910–918.

Sokal, R.R., and Rohlf, F.J. (1995). Biometry: The Principles and Practice of Statistics in Biological Sciences (W.H. Freeman Company).

Song, S., Sjöström, P.J., Reigl, M., Nelson, S., and Chklovskii, D.B. (2005). Highly nonrandom features of synaptic connectivity in local cortical circuits. PLoS Biol. *3*, e68.

Soodak, R.E. (1987). The retinal ganglion cell mosaic defines orientation columns in striate cortex. Proc. Natl. Acad. Sci. USA *84*, 3936–3940.

Stosiek, C., Garaschuk, O., Holthoff, K., and Konnerth, A. (2003). In vivo two-photon calcium imaging of neuronal networks. Proc. Natl. Acad. Sci. USA *100*, 7319–7324.

Tan, A.Y., Brown, B.D., Scholl, B., Mohanty, D., and Priebe, N.J. (2011). Orientation selectivity of synaptic input to neurons in mouse and cat primary visual cortex. J. Neurosci. *31*, 12339–12350.

Van Hooser, S.D., Heimel, J.A., Chung, S., Nelson, S.B., and Toth, L.J. (2005). Orientation selectivity without orientation maps in visual cortex of a highly visual mammal. J. Neurosci. *25*, 19–28.

van Vreeswijk, C., and Sompolinsky, H. (1996). Chaos in neuronal networks with balanced excitatory and inhibitory activity. Science *274*, 1724–1726.

van Vreeswijk, C., and Sompolinsky, H. (1998). Chaotic balanced state in a model of cortical circuits. Neural Comput. *10*, 1321–1371.

von der Malsburg, C. (1973). Self-organization of orientation sensitive cells in the striate cortex. Kybernetik *14*, 85–100.

Wang, X., Lu, T., Snider, R.K., and Liang, L. (2005). Sustained firing in auditory cortex evoked by preferred stimuli. Nature *435*, 341–346.

Webster, M.A., and De Valois, R.L. (1985). Relationship between spatial-frequency and orientation tuning of striate-cortex cells. J. Opt. Soc. Am. A *2*, 1124–1132.

Wilson, D.E., Whitney, D.E., Scholl, B., and Fitzpatrick, D. (2016). Orientation selectivity and the functional clustering of synaptic inputs in primary visual cortex. Nat. Neurosci. *19*, 1003–1009.

Zhao, X., Chen, H., Liu, X., and Cang, J. (2013). Orientation-selective responses in the mouse lateral geniculate nucleus. J. Neurosci. *33*, 12751–12763.

STAR★METHODS

KEY RESOURCES TABLE

REAGENT or RESOURCE	SOURCE	IDENTIFIER
Experimental Models: Organisms/Strains		
C57BL/6J mouse strain	Jackson Labs	000664
Software and Algorithms		
MATLAB 7.4.0	Mathworks (https://www.mathworks.com)	N/A

CONTACT FOR REAGENT AND RESOURCE SHARING

Further information and requests for resources and reagents should be directed to and will be fulfilled by the Lead Contact, David Hansel (david.hansel@parisdescartes.fr).

EXPERIMENTAL MODEL AND SUBJECT DETAILS

Mice

Experiments were conducted using normal, adult male and female C57 mice (n = 33, P34 - P60). All procedures were approved by The University of Texas at Austin Institutional Animal Care and Use Committee.

METHOD DETAILS

Detailed Experimental Methods

Physiology

Procedures for two-photon imaging and physiology were based on those previously described (Scholl et al., 2015, 2017). Mice were anesthetized with intraperitoneal injections of 1000 mg/kg urethane and 10 mg/kg chlorprothixene. Brain edema was prevented by intraperitoneal injection of up to 10 mg/kg dexamethasone. Animals were warmed with a thermostatically controlled heat lamp to maintain body temperature at 37°C. A tracheotomy was performed and the head was placed in a mouse adaptor (Stoelting). A craniotomy and duratomy were performed over visual cortex. Eyes were kept moist with a thin layer of silicone oil. Primary visual cortex was located and mapped by multi-unit extracellular recordings with tungsten electrodes (1 mΩ, Micro Probes). The V1/V2 boundary was identified by the characteristic gradient in receptive locations (Dräger, 1975; Métin et al., 1988). Eye drift under urethane anesthesia is typically small and results in a change in eye position of less than 2 degrees per hour (Sarnaik et al., 2014).

Dye Loading and In Vivo Two-Photon Microscopy

Bulk loading of a calcium sensitive dye under continuous visual guidance followed previous protocols in V1 (Golshani and Portera-Cailliau, 2008; Kerr et al., 2005; Mrsic-Flogel et al., 2007; Ohki et al., 2005; Stosiek et al., 2003). Dye solution contained 0.8 mM Oregon Green 488 BAPTA-1 AM (OGB-1 AM, Invitrogen) dissolved in DMSO (Sigma-Aldrich) with 20% pluronic acid (Sigma-Aldrich) and mixed in a salt solution (150 mM NaCl, 2.5 mM KCl, 10 mM HEPES, pH 7.4, all Sigma-Aldrich). 40-80 μM Alexa Fluor 594 (Invitrogen) was also included for visualization during and immediately after loading. Patch pipettes (tip diameter 2-5 μm, King Precision Glass) containing this solution were inserted into the cortex to a depth of 250-400 μm below the surface with 1.5% agarose (in saline) placed on top the brain. The solution was carefully pressure injected (100-350 mbar) over 10-15 minutes to cause the least amount of tissue damage. OGB-1-AM is only weakly fluorescent before being internalized, so the amount of dye injected was inferred through the red dye. To ensure full loading we waited 1 hour before adding a glass coverslip for imaging. Metal springs were fastened on the attached head plate to place pressure on the glass coverslip and reduce brain pulsations. Fluctuations in calcium fluorescence were collected with a custom-built two-photon resonant mirror scanning microscope (Scholl et al., 2015) and a mode-locked (925 nm) Chameleon Ultra Ti:Sapphire laser (Coherent). Excitation light was focused by a 16X or 40x water objective (0.8 numerical aperture, Nikon). Images were obtained with custom software (Labview, National Instruments). A square region of cortex 300 μm wide was imaged at 256x455 pixels. In all experiments, multiple focal planes, separated by 20-25 μm, were used to collect data, starting around 150 μm below the cortical surface. Before each experiment neuron drift was measured over a 2-3 min period. If drift occurred then the glass coverslip and agarose were readjusted to stabilize the brain during stimulus protocol (7-20 minutes each focal plane).

Stimuli

Visual stimuli were generated by a Macintosh computer (Apple) using the Psychophysics Toolbox (Brainard, 1997; Pelli, 1997) for MATLAB (Mathworks). Gratings were presented using a Sony video monitor (GDM-F520) placed 25 cm from the animal's eyes. The video monitors had a non-interlaced refresh rate of 100Hz,a spatial resolution of 1024x768 pixels, which subtended 40x30 cm, and a mean luminance of 40 cd/cm^2. Drifting gratings (38 deg diameter for imaging, variable diameter for electrophysiology, 0.01-0.04 spatial frequency, 100% contrast, 2 Hz temporal frequency) were presented for 2-3 s. Each stimulus was followed by a 3 s blank (mean luminance) period in the imaging protocol. Spontaneous activity was measured during blank (mean luminance) periods interleaved with drifting grating stimuli, all presented in a pseudorandom sequence. Direction presented ranged from 0-330 deg. Different spatial frequencies used were either presented individually in separate blocks (n = 15) or interleaved (n = 591) within the same block. Hartley stimuli were presented for each spatial frequency combination for 250 ms (Malone and Ringach, 2008; Ringach et al., 2016). For each spatial frequency combination four phases were presented and the response to these phases were averaged. These were repeated 5-30 times per cell. During imaging sessions, each stimulation protocol was repeated 7-10 times at each focal plane. For each orientation and spatial frequency data was recorded between 10 and 24 s. The microscope objective and photomultiplier tubes were shielded from stray light and the video monitors.

Detailed Computational Model of Mouse V1

The model is composed of two networks. One represents LGN and has N_L neurons. The second network represents layer 4 and layer 2/3 in mouse V1. For simplicity these two layers are collapsed into one single network, with N_E excitatory and N_I inhibitory neurons. In both networks the neurons are arranged on a square grid and the position (x_{iA},y_{iA}), where (i,A) denotes the neuron i = 1,...,N_A of population A = E,I,L. The position of neuron (i,A) is given by $x_{ia} = M(i_x/\sqrt{N_A}); y_{ia} = M(i_y/\sqrt{N_A})$ where M is the size of the network (2mm), $i_x = (i-1) mod \sqrt{N_A}$ and $i_y = (i-1)/\sqrt{N_A}$. Here x is the largest integer equal to or smaller than x. All N_A are square integers so that i_x and i_y are integers between 0 and $\sqrt{N_A} - 1$. Unless said otherwise we take N_E = 32400, N_I = 8100, N_L = 25600.

Cortical Neurons

They are described in terms of conductance-based models. The membrane potential of neuron (i,A), A = E,I, evolves in time according to

$$C\frac{dV_{iA}}{dt} = -I_{l,iA} - I_{Na,iA} - I_{K,iA} - I_{adapt,iA} + I_{LGN,iA} + I_{rec,iA} + I_{b,iA} \quad (1)$$

where C is the membrane capacitance, $I_{l,iA}$, is the leak current, and $I_{Na,iA}$, $I_{K,iA}$ are the intrinsic sodium and potassium currents that shape the action potentials and $I_{adapt,iA}$ is an adaptation potassium current which included in E neurons, only. The dynamics of these currents are as in (Hansel and van Vreeswijk, 2012). The current $I_{LGN,iA}$ describes the input from LGN, $I_{rec,iA}$ is the recurrent input from other cortical neurons and $I_{back,\ iA}$ represents a background input from other cortical regions not explicitly included in the model.

LGN Neurons

LGN cells are modeled as Poisson neurons with time varying rates that depend on the visual stimulus. Neuron (i,L) responds to a luminosity field L(x,y,t) with an instantaneous firing rate

$$r_{iL}(t) = \left[r_0 + \iint dxdy R_{il}(x,y) L(x,y,t) \right]_+ \quad (2)$$

where r_0 is the spontaneous firing rate of the neuron, assumed to be the same for all LGN cells, $R_{iL}(x,y)$ is its receptive field and $[x]_+ = x$ for $x > 0$, $[x]_+ = 0$ for $x < 0$. The luminosity field of a sinusoidal drifting grating with orientation θ, spatial wavelength λ, and temporal frequency ω, is

$$L(x,y,t) = L_0 \left[1 + \varepsilon \cos\left(k_x x + k_y y - \omega t \right) \right] \quad (3)$$

where L_0 is the average luminosity, ε is the contrast, and the wave-vector of the grating is: $\boldsymbol{k} = (k_x, k_y) = (k\cos\theta, k\sin\theta)$ with $k = 2\pi/\lambda$. The parameters used in our simulations are listed in Tables S1 and S2.

The receptive field of neuron (i,L) has the form

$$R_{il}(x,y) = \pm R \left[\frac{\exp\left(-\frac{x'^2}{2\sigma_{cx}^2} - \frac{y'^2}{2\sigma_{cy}^2} \right)}{2\pi\sigma_{cx}\sigma_{cy}} - \beta \frac{\exp\left(-\frac{x'^2}{2\sigma_{sx}^2} - \frac{y'^2}{2\sigma_{sy}^2} \right)}{2\pi\sigma_{sx}\sigma_{sy}} - \frac{U}{S} \right] \quad (4)$$

where $x' = (x - x_{il})\cos\theta_{iL} + (y - y_{il})\sin\theta_{iL}$, $y' = -(x - x_{il})\sin\theta_{iL} + (y - y_{il})\cos\theta_{iL}$, β is a parameter that controls the relative weights of the two subfields, R is a constant (1 Hz). U is a constant such that $\iint_S dx\, dy\, R_{il}(x,y) = 0$. The integral is performed over a surface of size S that is much larger than the size of the network. The long and short axis of the center (resp. surround) region are denoted here by σ_{cx} and σ_{cy} (resp. σ_{sx} and σ_{sy}). The global sign is +1 if the receptive field is ON center and -1 if it is OFF center. We take this sign at random with equal probability to be +1 or -1.

In all simulations except those in Figure S7 we assume circular receptive fields for both center and surround subfields. In the simulations described in Figure S7 surrounds are circular but centers are elongated. We use the following parametrization: $\sigma_{cx}=\sqrt{1+\alpha}\sigma,\ \sigma_{cy}=(\sigma/\sqrt{1+\alpha}),\sigma_{sx}=\sigma_{sy}\equiv\sigma_s$ with $\sigma\equiv\sqrt{\sigma_{cx}\sigma_{cy}}$. Therefore, $\alpha=0$ corresponds to a circular center and surround subfields. In this case the LGN cell is not selective to orientation. The degree of selectivity increases with α.

The response of the LGN cells to a drifting grating can then be calculated based on

$$r_{iL}(t)=[r_0+\varepsilon\widehat{r}_{iL}(\theta,\lambda)\cos(\omega t-\Delta_{iL}(\theta,\lambda))]_+ \tag{5}$$

where, in the limit of large S,

$$\widehat{r}_{iL}(\theta,\lambda)=RL_0\left[\exp\left(-\frac{(k\sigma)^2(A+B\cos 2(\theta-\theta_{iL}))}{2}\right)-\beta\exp\left(-\frac{(k\sigma_s)^2}{2}\right)\right] \tag{6}$$

with $A=(\tilde{\alpha}^2+1)/2\tilde{\alpha}$ and $B=(\tilde{\alpha}^2-1)/2\tilde{\alpha}$, with $\tilde{\alpha}=1+\alpha$

The phase $\Delta_{iL}(\theta,\lambda)$ is: $\Delta_{iL}(\theta,\lambda)=2\pi(x_{iL}\cos\theta+y_{iL}\sin\theta)/\lambda$ ($\Delta_{iL}(\theta,\lambda)=\pi+2\pi(x_{iL}\cos\theta+y_{iL}\sin\theta)/\lambda$) for an ON (OFF) cell.

Thalamo-cortical and Recurrent Connectivity

The connectivity between model LGN and cortex is random and does not depend on the functional properties of the cells. The probability that cortical neuron (i,A) is connected to LGN cell (j,L) is

$$P_{ij,AL}=K_{AL}G(x_{iA}-x_{jL},\sigma_{AL})G(y_{iA}-y_{jL},\sigma_{AL}) \tag{7a}$$

where K_{AL} is the mean number of LGN inputs received by a cortical cell in population A and

$$G(x,\sigma)=\frac{1}{\sqrt{2\pi\sigma^2}}\sum_{k,l=-\infty}^{+\infty}\exp\left(-\frac{[x-Mk]^2}{2\sigma^2}\right) \tag{7b}$$

is the periodic Gaussian with variance σ^2.

The recurrent interactions in the cortical network are also random and non specific. The probability of connection between neuron (j,B) and (i,A) (A = E,I; B = E,I) is

$$P_{ij,AB}=K_{AB}G(x_{iA}-x_{jB},\sigma_{AB})G(y_{iA}-y_{jB},\sigma_{AB}). \tag{8}$$

The Feedforward and Recurrent Synaptic Currents

Thalamo-cortical synapses on cortical population A are all excitatory, have a reversal potential V_E, a strength g_{AL} and a synaptic time constant τ_L. The thalamo-cortical current, $I_{LGN,iA}$, in neuron (i,A) is

$$I_{LGN,\,iA}(t)=-g_{iL}(t)[\rho(V_{iA}-V_E)+(1-\rho)(V_L-V_E)] \tag{9}$$

with: $g_{iL}(t)=(g_{AL}/\tau_L)\sum_{j=1}^{N_L}C_{ij}^{AL}\sum_k\exp(-(t-t_{k,j})/\tau_L)$, where C^{AL} is the N_AXN_L connectivity matrix of the thalamo-cortical projections ($C_{ij}^{AL}=1$ if there is a connection from neuron (j,L) to neuron (i,A); $C_{ij}^{AL}=0$ otherwise), and $t_{k,j}$ is the time of the k-th spike generated by neuron (j,L). The sum over k is over all the spikes with $t_{k,j}<t$.

The total recurrent current into neuron (I,A) is $I_{rec,iA}=I_{iA,E}+I_{iA,I}$ where

$$I_{iA,B}=-g_{iA,B}(t)[\rho(V_{iA}-V_B)+(1-\rho)(V_B-V_L)] \tag{10}$$

with $g_{iA,B}(t)=(g_{AB}/\tau_{AB})\sum_{j=1}^{N_L}C_{ij}^{AB}\sum_k\exp(-(t-t_{k,j})/\tau_{AB})$.

Finally, the background current in Equation (1) is modeled as

$$I_{b,iA}=-g_{b,iA}(t)[\rho(V_{iA}-V_E)+(1-\rho)(V_L-V_E)] \tag{11}$$

where $g_{b,iA}(t)$ is a random Gaussian variable with mean $K_bg_br_0$ and variance $\sqrt{K_b}g_br_0$. This represents the effect of K_b uncorrelated Poisson inputs, each of synaptic strength g_b.

Note that in Equations (9,10) the right hand-sides comprise two contributions. The first is proportional to the driving force $V_{iA}-V_B$. Thus it modifies the input conductance of the neuron. This contrasts with the second contribution which does not depend on the membrane potential of the post-synaptic cell. We adopted this description to incorporate in a simplified manner the fact that the change in input conductance induced by a synapse depends on its location on the dendritic tree. Proximal synapses which substantially affect the neuron's input conductance are represented by the first contribution. The second contribution accounts for the synapses which are distal and which affect the input conductance of the neuron less (see also Hansel and van Vreeswijk, 2012).

QUANTIFICATION AND STATISTICAL ANALYSIS

Experimental Analysis

Two-Photon Calcium Imaging Analysis

Images were analyzed with custom MATLAB software (Mathworks). Cells were identified by hand from structure images based on size, shape, and brightness. Cell masks were generated automatically following previous methods (Nauhaus et al., 2012). Glia were easily avoided due to their different morphology from both OGB-1 AM filled neurons. Time courses for individual neurons were extracted by summing pixel intensity values within cell masks in each frame. Responses (F_t) to each stimulus presentation were normalized by the response to the gray screen (F_0) immediately before the stimulus came on:

$$\Delta F/F = (F_t - F_0)/F_0.$$

For each stimulus, the mean change in fluorescence $\Delta F/F$ was calculated from a 0.66 s window of the response centered at the time of the global peak to all visual stimuli. Visually responsive cells were required to fulfill 4 criteria in order for them to be included in our analysis. First, the response to the preferred orientation was significantly different than the spontaneous response (t test for unequal variances, $p < 0.05$). Second, the response amplitude must be greater than 8% $\Delta F/F$. Third, responses were required to have distinct different trial-to-trial fluorescence time courses, as determined by measuring the type II regression of the time course of each cell's response and the neuropil response, extracting the slope of that relationship and determining if it was significantly different from unity (Sokal and Rohlf, 1995). Finally we restricted our analysis to cells with OSI greater than 0.08 at the spatial frequencies being compared. Fewer cells meet our inclusion criteria for comparison of 0.01 cyc/deg to 0.04 cyc/deg (8%) than 0.02 cyc/deg to 0.04 cyc/deg (40%). Mean changes in fluorescence from visually responsive neurons were used to generate tuning curves for orientation selectivity. 95% confidence intervals (CI) were generated on the preferred orientation of the neurons at different spatial frequencies using method described below. The mean CI length on preferred orientation for 0.04 cyc/deg was 5.1 degrees whereas for 0.01 cyc/deg it was 6.4 degrees and the distributions of CI are not significantly different (unpaired t test, $p < 0.5$).

Electrophysiology Analysis

Spiking responses for each stimulus were cycled-averaged across trials after removing the first cycle. The Fourier transform of mean cycle-average responses was used to calculate the mean (F0) and modulation amplitude (F1) of each cycle-averaged response, after mean spontaneous activity was subtracted. The subthreshold membrane potential responses were also similarly computed after median filtering the voltage traces to remove spikes. Peak responses were defined as the sum of the mean and modulation (F0 + F1).

Peak responses per trial across each condition for neuronal responses measured using electrophysiology and imaging were bootstrapped to compute the vector average orientation (number of bootstrap resamples = 10000). This was used as the preferred orientation for the neuron. For electrophysiology, cells were only included in the analysis, if the bootstrapped confidence intervals on mean of the maximum amplitude spiking response (number of bootstrap resamples = 10000) did not include zero. A double Gaussian curve was fit to the responses for characterizing orientation tuning (Carandini and Ferster, 2000):

$$R(\theta) = \alpha e^{-\left(\theta-\theta_{pref}\right)^2/\left(2\sigma^2\right)} + \beta e^{-\left(\theta-\theta_{pref}+\pi\right)^2/\left(2\sigma^2\right)} + k.$$

Here $R(\theta)$ is the response of the neuron to different orientations (θ), σ is the width of the tuning curve, k is the mean background activity, α and β are peak amplitudes, and θ_{pref} is the orientation preference. Gaussian fits were used only for qualitative description of the tuning. The actual fit parameters have not been used in the analysis. The orientation selectivity index was also computed (Ringach et al., 2002; Tan et al., 2011):

$$OSI = \frac{\sqrt{\left(\sum R(\theta)\sin(2\theta)\right)^2 + \left(\sum R(\theta)\cos(2\theta)\right)^2}}{\sum R(\theta)}.$$

The circular correlation (cc) between the preferred orientations (PO) is defined as:

$$cc = \frac{\sum_{i,j}\sin(PO_i - PO_j)\sin\left(PO_i' - PO_j'\right)}{\sqrt{\sum_{i,j}\sin^2(PO_i - PO_j)\sum_{i,j}\sin^2\left(PO_i' - PO_j'\right)}}$$

where PO_i is the preferred orientation of neuron i for one spatial frequency and PO'_i is the preferred orientation of the same neuron for another spatial frequency. This number is always in the range [-1:1], reaching 1 for perfect linear correlation between the preferred orientations in the two conditions. 95% confidence intervals are generated on the circular correlation using bootstrapping (Sokal and Rohlf, 1995) (number of bootstrap resamples = 10000).

Statistical Analysis

For both calcium data and electrophysiological data we determined if the difference in the preferred orientations estimated at different spatial frequencies was statistically significant using the studentized method of generating 95% confidence intervals (Sokal and Rohlf, 1995). The same method was used for generating 95% confidence intervals on the circular correlation.

Model Analysis

Numerical Procedures and Analysis

Numerical simulations were performed using a 4th-order Runge-Kutta scheme to integrate the neuronal dynamics (Press, 1992). The synaptic interactions and the noise were treated at first order. The time step is $\delta t = 0.05ms$.

For each cortical neuron the mean firing rate, $F_0(\theta_k)$, and firing rate temporal modulation (first Fourier component of the response) $F_1(\theta_k)$ were estimated for each orientation, $\theta_k = (k-1)20^\circ, k = 1,..,9$, by averaging the response upon 40 s of stimulation, unless specified otherwise. We then computed the orientation averaged responses

$$\overline{F}_n = \frac{1}{9}\sum_{k=1}^{9} F_n(\theta_k) \quad n = 0,1$$

and the complex numbers

$$Z_n = \frac{1}{9}\sum_{k=1}^{9} F_n(\theta_k) e^{2i\theta_k} \quad n = 0,1.$$

The Orientation Selectivity Index (OSI) and the Preferred Orientation (PO) of the peak response is then estimated from

$$OSI = \frac{|Z_0 + Z_1|}{\overline{F}_0 + \overline{F}_1}$$

$$PO = Arg(Z_0 + Z_1).$$

The OSI is 0 if the response has no tuning and 1 if the neuron responds at only one orientation. These definitions for the OSI and PO are equivalent to those used in the analysis of the experimental data (see above).

The definition of correlation coefficient is same as described above.

We also fit the tuning curves of the mean, $F_0(\theta)$, and temporal modulation, $F_1(\theta)$, of the spike to periodic Gaussian functions

$$\widetilde{F_n}(\theta) = A_n + B_n \sum_{kJ=-\infty}^{+\infty} \exp\left(-\frac{\left[\theta - k\pi - \widehat{\theta}_n\right]^2}{2\sigma_n^2}\right)$$

with n = 0,1. We estimated the parameters $A_n, B_n, \widehat{\theta}_n, \sigma_n$, for each neuron by minimizing the quadratic error: $E(A_n, B_n, \widehat{\theta}_n, \sigma_n) = (1/9)\sum_{k=1}^{9}(\widetilde{F_n}(\theta_k) - F_n(\theta_k))^2$.

Robustness of the Results

To check that a time step, $\delta t = 0.05ms$, was sufficiently small, we also performed several simulations with $\delta t = 0.025ms$. To verify that our results were also robust to changes in system size we performed several simulations on networks with N_E = 78560, N_I = 19600, N_L = 40000, keeping the average number of connections into E and I cells the same.

Structure of the ON and OFF Subfield of the Thalamic Input

We characterized the thalamo-cortical input in the model by performing simulations with a protocol similar to the one in the experiments of Lien and Scanziani (2013). The stimuli used to map the receptive fields were Gaussian spots with a standard deviation of 5.6 degrees. The spots were presented in one of 64 locations arranged regularly in a square of 8x8 in the center of the network. The distance between the centers of adjacent spots was 7°. In order to characterize both ON and OFF receptive fields the stimuli were either brighter or dimmer than the background illumination. Each stimulus was presented during 1sec. During that time we evaluated the average of the conductance of the thalamic to each cortical neuron. We checked that the results were robust with respect to longer simulation times. The intensity of the stimulus (with respect to the background value) at the center of the Gaussian was $I_0 = \pm 0.075$. After performing the simulations, the centers of the ON and OFF subfields were estimated by evaluating their center of mass: $< \mathbf{r} > = \Sigma_i f_i \mathbf{r}_i / \Sigma_i f_i$, where f_i is the average thalamic input for a stimulus at position is $\mathbf{r}_i$. In order to reduce the noise level we performed the sum only over the locations for which the average input is larger or equal than 30% of the maximal average input.

Let us note that this way of estimating the center of the fields is only valid for cortical neurons whose feedforward inputs do not come from the border of the LGN network. Otherwise, because of the periodic boundary conditions of the LGN receptive fields, the linear estimation could combine inputs from opposite sides of the visual field. As the feedforward connectivity profile is topographically organized, neurons in the center of the cortex receive inputs from neurons in the center of the LGN. Therefore, boundary effects can be avoided by evaluating the center of mass only for neurons in the central part of the cortical network. In particular all the statistics of the ON and OFF subfields were estimated from neurons the square region of 14°x14° at the center of the network (361 neurons).

Parameters of the Computational Model

The cortical network is assumed to have a size of 2mm x 2mm representing 140°x 140° in the visual field (Kalatsky and Stryker, 2003).

The synaptic dispersion of the recurrent connectivity is taken to be 200 μm, consistently with values reported in Reyes and Sakmann (1999). Unless indicated otherwise, the dispersion of the feed-forward connectivity was 100 μm.

The synaptic efficacies were as in Table S1. With these parameter values post-synaptic potentials have peak size is 0.5 mV (E- > E interaction), −0.3 mV (I- > E), 2.7 mV (E- > I), −0.9 mV (I- > I), 0.9 mV (LGN- > E), 0.8 mV (LGN- > I). See Figure S1A.

We introduced heterogeneity in the parameters σ_{cx}, σ_{sx}, α,β. For each thalamic neuron these parameters were chosen from a log-normal distribution

$$P(x) = \frac{1}{xs\sqrt{2\pi}} e^{-\frac{(\ln x - m)^2}{2s^2}},$$

where the parameters m and s are given by σ_{cxm}, σ_{cxs}, σ_{sxm}, σ_{sxs}, α_m, α_s, β_m, β_s respectively. The values of these parameters are given in Table S2. Examples of receptive fields of LGN neurons in the model are plotted in Figure S1B. The heterogeneity in the LGN receptive fields is depicted in Figure S1C.

In the simulations of Figure S7, the preferred orientations of LGN neurons are chosen randomly with a distribution

$$P(\theta) = P_0 \left[a_\theta + b_\theta \exp\left(-\frac{\theta^2}{2c_\theta^2} \right) \right],$$

where P_0 is a normalization constant. The parameters we used in these simulations are given in Table S3.